Atmos. Chem. Phys. Discuss., 13, 8023–8064, 2013
www.atmos-chem-phys-discuss.net/13/8023/2013/
doi:10.5194/acpd-13-8023-2013

Atmospheric Chemistry and Physics Discussions

On the consistency between global and regional methane emissions inferred from SCIAMACHY, TANSO-FTS, IASI and surface measurements

C. Cressot[1], F. Chevallier[1], P. Bousquet[1], C. Crevoisier[2], E. J. Dlugokencky[3], A. Fortems-Cheiney[1], C. Frankenberg[4], R. Parker[5], I. Pison[1], R. A. Scheepmaker[6], S. A. Montzka[3], P. B. Krummel[7], L. P. Steele[7], and R. L. Langenfelds[7]

[1]Laboratoire des Sciences du Climat et de l'Environnement, UMR8212, 91191 Gif-sur-Yvette, France
[2]Laboratoire de Météorologie Dynamique/CNRS/IPSL, Ecole Polytechnique, Palaiseau, France
[3]Climate Monitoring and Diagnostics Laboratory, NOAA, Boulder, Colorado, USA
[4]Jet Propulsion Laboratory, California Institute of Technology, Pasadena, California, USA
[5]Earth Observation Science, Space Research Centre, University of Leicester, Leicester, UK
[6]SRON Netherlands Institute for Space Research, Utrecht, the Netherlands
[7]Centre for Australian Weather and Climate Research, CSIRO Marine and Atmospheric Research, Aspendale, Victoria, Australia

Received: 22 February 2013 – Accepted: 4 March 2013 – Published: 25 March 2013

Correspondence to: C. Cressot (cindy.cressot@lsce.ipsl.fr)

Published by Copernicus Publications on behalf of the European Geosciences Union.

ACPD
13, 8023–8064, 2013

Abstract

Satellite retrievals of methane weighted atmospheric columns are studied within a Bayesian inversion system to infer the global and regional methane emissions and sinks. 19-month inversions from June 2009 to December 2010 are independently computed from three different space-borne observing systems under various hypotheses for prior-flux and observation errors. Posterior methane emissions are inter-compared and evaluated with surface mole fraction measurements, via a chemistry-transport model. Sensitivity tests show that refining the assigned error statistics has a larger impact on the quality of the inverted fluxes than correcting for residual airmass-factor-dependent biases in the satellite retrievals. Improved configurations using TANSO-FTS, SCIAMACHY, IASI and surface measurements induce posterior methane global budgets of respectively, $568 \pm 17\,\mathrm{Tg\,yr^{-1}}$, $603 \pm 28\,\mathrm{Tg\,yr^{-1}}$, $524 \pm 16\,\mathrm{Tg\,yr^{-1}}$ and $538 \pm 20\,\mathrm{Tg\,yr^{-1}}$ over the one-year period August 2009–July 2010. This consistency between some of these satellite retrievals and surface measurements is promising for future improvement of CH_4 emission estimates by inversions.

1 Introduction

Methane (CH_4) is the second most important anthropogenic greenhouse gas in terms of radiative forcing after carbon dioxide (Forster, 2007). CH_4 sources are of biogenic origin (wetlands, rice cultivation, ruminant animals, termites, landfills and waste), of pyrogenic origin (biomass burning) and of thermogenic origin (production, transport and distribution of fossil fuels, geological leakages). The emissions are about 2/3 anthropogenic and 1/3 natural, with large uncertainties for each individual source (20–100 %). Its loss in the atmosphere is mainly controlled by the chemical reaction with hydroxyl free radical (OH) and its lifetime spans about 9 yr. Methane concentrations have reached unprecedented values since the beginning of the industrial era (+150 %) and the explanation of their recent variability is still debated (Bousquet et al., 2011;

ACPD
13, 8023–8064, 2013

Rigby et al., 2008). Methane sources and sinks are classically estimated either using bottom-up approaches (process-based modeling and inventories) or top-down approaches (atmospheric inversions). Atmospheric inversions have shown to improve bottom-up methane emission estimates from global to regional scales, mostly based so far on surface CH_4 observations. Since 2003, retrievals of methane weighted atmospheric columns from space are available, largely increasing the number of available constraints for atmospheric inversions, at the cost of a lower individual precision on measurements ($\sim 2\,\%$) as compared to surface observations ($\sim 0.2\,\%$).

We study four different observing systems that measure or retrieve CH_4 mole fractions (nmol mol^{-1}, abbreviated ppb): the SCanning Imaging Absorption spectroMeter for Atmosphere CartograpHY (SCIAMACHY) onboard the ENVIronment SATellite (ENVISAT), the Thermal And Near infrared Sensor for carbon Observation- Fourier Transform Spectrometer (TANSO-FTS) onboard the Greenhouse Gas Observing SATellite (GOSAT), the Infrared Atmospheric Sounding Interferometer (IASI) onboard the Meteorological Operational Polar satellite (MetOp) and surface air sample sites from various networks (National Oceanic and Atmospheric Administration (NOAA), the Italian National Agency for New Technology, Energy and the Environment (ENEA), Japan Meteorological Agency (JMA), Commonwealth Scientific and Industrial Research Organisation (CSIRO), the National Institute of Water and Atmospheric Research (NIWA)). These observations do not have the same spatial (horizontal but also vertical) resolution nor the same space-time sampling, and therefore they are not easy to compare directly. We use the transport model of the Laboratoire de Météorologie Dynamique (LMDz4) coupled with the Simplified Assimilation Chemical System (SACS) to invert the methane fluxes from each dataset on a spatial grid of $3.75^\circ \times 2.5^\circ$ with a weekly temporal resolution. SACS allows combining methane observations and methyl-chloroform (CH_3CCl_3, called MCF hereinafter) observations to simultaneously optimize the emissions and oxidation of CH_4. We compare the posterior methane emissions and losses inferred from the various observing systems at both global and regional scales. Although the Tropics are not well covered by surface sites, the inversion

ACPD
13, 8023–8064, 2013

that assimilates surface measurements is taken here as the reference to evaluate the satellite products.

The theoretical framework used to infer methane emissions and their uncertainties is presented in Sect. 2. The data sets from the various observing systems used in this study are detailed in Sect. 3. Results from sensitivity tests introducing a bias correction on the satellite retrievals as a function of the airmass factor, the tuning of the input error statistics and the combination of satellite and surface CH_4 measurements in the inversion, are presented in Sect. 4 and discussed in Sect. 5.

2 Method

2.1 Inversion system

Our inversion scheme relies on Bayes' theorem and is based on a variational data assimilation system that has been detailed by Chevallier et al. (2005). The variational formulation of data assimilation provides a powerful technique when the dimension of the observation vector is very large, which is the case with satellites, and when the number of variables to be optimized is large as well, which is the case for grid-point-scale inversions. High-resolution inversions avoid some of the aggregation errors that hit low-resolution inversions (Bocquet et al., 2011; Kaminski et al., 2001). Variational data assimilation consists in minimizing a cost function J defined as follows:

$$J(\boldsymbol{x}) = \frac{1}{2}(\boldsymbol{x} - \boldsymbol{x}^{\mathrm{b}})^T \mathbf{B}^{-1}(\boldsymbol{x} - \boldsymbol{x}^{\mathrm{b}}) \quad (1)$$

$$+ \frac{1}{2}(H(\boldsymbol{x}) - \boldsymbol{y})^T \mathbf{R}^{-1}(H(\boldsymbol{x}) - \boldsymbol{y}); \quad (2)$$

$\boldsymbol{x}$ is the state vector that contains the variables to be optimized during the inversion process: the time series of weekly grid-point emission fluxes of CH_4 and MCF, together with their initial conditions (in the form of 2-D scaling factors on the CH_4 and MCF

ACPD
13, 8023–8064, 2013

columns) and time series of weekly scaling factors of OH column concentrations averaged into four bands of latitude (−90°/90°, −30°/0°, 0°/30°, 30°/90°). The vector $\boldsymbol{x}^{\mathrm{b}}$ represents the prior state of $\boldsymbol{x}$, the error statistics of which are defined by the covariance matrix **B**. Likewise, the vector $\boldsymbol{y}$ contains the observations of CH_4 and MCF mole fractions with their associated errors described by the covariance matrix **R**. Observation errors are defined with respect to the inversion system and therefore combine measurement errors, errors of the chemistry-transport model and representativity errors. The covariance matrix **R** is assumed diagonal to simplify calculations, meaning that no correlations between the observations are explicitly taken into account. Following Chapnik et al. (2006) and Chevallier (2007), the variances in **R** are inflated to account for the missing correlations. H is the non-linear observation operator that projects the state vector $\boldsymbol{x}$ onto the observation space. It contains the LMDz-SACS model presented in Sect. 2.4 and appropriate observation averaging kernels or weighting functions associated with the satellite retrievals.

The iterative minimizing process implies calculating the gradient of the cost function, which is implemented using the adjoint technique. The gradient of J can be written as follows:

$$\nabla J(\boldsymbol{x}) = \mathbf{B}^{-1}(\boldsymbol{x} - \boldsymbol{x}^{\mathrm{b}}) + \mathbf{H}^{T}\mathbf{R}^{-1}(H(\boldsymbol{x}) - \boldsymbol{y}); \quad (3)$$

where **H** is the tangent linear of the observation operator H which is calculated at each iteration. The inversion process is iteratively solved with the M1QN3 algorithm developed by Gilbert and Lemaréchal (1989) until the gradient norm gets reduced by more than 99 %. It provides the statistically-optimal solution given the observations, the prior information and their respective uncertainties (i.e. the maximum of the posterior probability density function), but not directly the uncertainties associated with this solution. In fact, these uncertainties can be estimated by calculating the Hessian matrix but this is practically very costly given the dimension of the state vector. Instead, we use a robust Monte-Carlo approach to compute the posterior uncertainties (Chevallier et al., 2007). This method consists in performing several inversions with randomly

ACPD
13, 8023–8064, 2013

perturbed observations and priors according to their respective error statistics. Because the estimation of the posterior uncertainties seems to become stable from 8 inversion-members (not shown), an ensemble of 10 19-month inversions is assumed to be enough to produce an ensemble of solutions well representing the dispersion around the optimal solution $\boldsymbol{x}_a$. It completes the description of the posterior distribution for aggregated values (typically regional and annual). The improvement on methane emissions brought by an inversion is characterized by the uncertainty reduction, defined as one minus the ratio between posterior and prior uncertainties.

2.2 Bias correction

In a previous inversion study, Bergamaschi et al. (2009) proposed a bias correction as a function of the latitude and of the month for SCIAMACHY. Here, we parameterize possible biases of SCIAMACHY and TANSO-FTS as a function of the airmass factor A_F. A_F is a parameter varying with the latitude as well, but it has the advantage of directly accounting for the geometrical position of the observing satellite and of the sun.

$$A_F = \frac{1}{\cos(\theta)} + \frac{1}{\cos(\xi)}; \tag{4}$$

where θ represents the solar zenith angle and ξ the angle of view of the satellite. The optimized 4-D CH_4 state obtained from the inversion using surface measurements is considered as our reference. We linearly regress the difference between this optimized state and the satellite observations of TANSO-FTS and SCIAMACHY against A_F for the 19-month period at once. With 2 parameters only, estimated from the 19 months of the reference inversion with seasonally-varying data coverage, we still consider our reference to be independent from the other inversions for the quantities studied in the following. Likewise, this regression does not necessarily improve the quality of the retrieved global annual growth rate.

ACPD
13, 8023–8064, 2013

2.3 Tuning error statistics

We use the method of Desroziers et al. (2006) to develop simple diagnostics about the error variances of the observations, of the prior and of the analysis in the observation space. In principle, this method is an iterative process in which **B** and **R** are tuned from the following equations until convergence:

$$E[(H(\boldsymbol{x}_a) - H(\boldsymbol{x}_b))(y - H(\boldsymbol{x}_b))^T] = \mathbf{HBH}^T \quad (5)$$

$$E[(y - H(\boldsymbol{x}_a))(y - H(\boldsymbol{x}_b))^T] = \mathbf{R} \quad (6)$$

$$E[(y - H(\boldsymbol{x}_b))(y - H(\boldsymbol{x}_b))^T] = \mathbf{HBH}^T + \mathbf{R} \quad (7)$$

$$E[(H(\boldsymbol{x}_a) - H(\boldsymbol{x}_b))(y - H(\boldsymbol{x}_a))^T] = \mathbf{HAH}^T \quad (8)$$

Practically, this iterative process is very costly with our inversion system. In fact, Eqs. (5)–(8) need the implementation of the inversion, of which the error statistics are diagnosed, and the implementation of the complete Monte-Carlo study associated (i.e. 10 more perturbed inversions see Sect. 2.1). In this study, only one iteration of these diagnostics is implemented for each inversion. Equations (5)–(8) are applied here on the ensemble defined by all observations at once for the period June 2009–December 2010. In doing so, both sides of the equations are scalar values. These equations allow calculating the observation error variances ($\mathrm{var_o}$), prior variances ($\mathrm{var_b}$), full variances ($\mathrm{var} = \sqrt{(\mathrm{var_o^2} + \mathrm{var_b^2})}$) and analysis variances ($\mathrm{var_a}$) that are defined in our system. The values $\mathrm{diag_o}$, $\mathrm{diag_b}$, diag and $\mathrm{diag_a}$ respectively represent the diagnosed values for the observations, the prior, the full and the analysis variances. The ratio ($\mathrm{ratio} = \frac{\mathrm{diag}}{\mathrm{var}}$) is an indicator of the goodness of the variances used in our inversions and, in the best case, equals one. These diagnostics can be advantageously extended to tune the error correlations. However, this implies defining retrieval ensembles for each correlation lag, in spite of irregular space-time sampling; this is not attempted here.

ACPD
13, 8023–8064, 2013

2.4 Chemistry-Transport Model

The inversion scheme includes a chemistry-transport model (CTM) that combines the LMDz4 transport model (Hourdin et al., 2006) in a nudged (towards analyzed winds) and offline (transport mass fluxes are precomputed) mode, and the chemistry module SACS implemented by Pison et al. (2009) to estimate the methane emissions that most likely generated the observed mole fractions. The SACS module accounts for the interactions between CH_4, OH and MCF. Indeed, MCF only reacts with OH, which controls 90 % of the destruction of CH_4 in the troposphere. Measurements of MCF mole fractions, the emissions of which are relatively well known, are used to constrain the OH modeled mole fractions. CH_4 and MCF mole fractions are synergistically optimized during the inversion process to estimate the methane surface sources and the methane atmospheric sink on a spatial grid of $3.75^\circ \times 2.5^\circ$ and weekly temporal resolution.

3 Prior information and observations

3.1 Prior information

Our system exploits some prior information $\boldsymbol{x}_b$ which combines different standard and recent inventories (Table 1). The anthropogenic emissions of CH_4 are drawn from the Emission Database for Global Atmospheric Research EDGAR-v4.2 (Olivier and Berdowski, 2001) and biomass burning emissions were from the interannual Global Fire and Emission Database GFED-v3 (van der Werf et al., 2010), both valid for 2008. No effort is made here to adapt these inventories to the years of the study (2009 and 2010). Other sources are added to these emissions: termites from a study of Sanderson (1996), ocean from Lambert and Schmidt (1993) and wetlands from Kaplan (2002). Soil uptake is based on Ridgwell et al. (1999). The 3-D production of OH is obtained from a previous simulation of the full atmospheric chemistry model LMDz-INCA (Hauglustaine et al., 2004). MCF emissions are described by the EDGAR-v3.2

ACPD
13, 8023–8064, 2013

database and are extrapolated for the years 2009 and 2010 based on a former atmospheric inversion (Bousquet et al., 2005), which has been updated.

Large uncertainties are associated to CH_4 emissions especially because emissions in wetlands are highly uncertain. For instance, current bottom-up inventories range between 223 $Tg\,yr^{-1}$ and 469 $Tg\,yr^{-1}$ for the global methane natural sources and between 296 $Tg\,yr^{-1}$ and 353 $Tg\,yr^{-1}$ for the global methane anthropogenic sources (Kirschke et al., 2013). The standard deviation of the errors of grid-point weekly CH_4 prior emissions are defined as a percentage (120 %) of the maximum value of the prior emissions between the 8 nearest neighbors in the corresponding month for each grid point (Pison et al., 2009). Errors on OH scaling factors are set at ±10 % and those on MCF are set at ±1 % of the flux (from now on, the ± sign is used to represent standard deviations). MCF errors are relatively small because their emissions are considered to be well known, which motivates their use to constrain the OH concentrations. Errors on the initial conditions are set at ±10 % for MCF fluxes and ±3 % for CH_4 fluxes. All error spatial correlations are defined by an e-folding length of 500 km over land and of 1000 km over sea, without any correlation between land and ocean grid points. Temporal error correlations are all defined by an e-folding length of 2 weeks. Combining variances and correlations, the CH_4 prior emissions budget amounts to $554 \pm 53\,Tg\,yr^{-1}$, which is consistent with the large range seen among the current bottom-up inventories (Kirschke et al., 2013). This matrix will be further tuned in Sect. 4.3.1 based on the objective diagnostics described in Sect. 2.3: a multiplicative factor α is estimated so that the new covariance matrix $\alpha\mathbf{B}$ satisfies Eq. (5).

3.2 Surface measurements

Pointwise methane surface measurements are sparsely distributed but provide observations of the dry air mole fractions with high accuracy and precision (0.2 %). We have selected 49 sites that had regular measurements during the period June 2009–December 2010 (Fig. 1) from the NOAA global cooperative air sampling network (Dlugokencky et al., 1994, 2009), JMA (Matsueda et al., 2004), ENEA (Artuso et al., 2007),

ACPD
13, 8023–8064, 2013

CSIRO (Francey et al., 1999) and NIWA (Lowe et al., 1991) networks. The synoptic variability from GLOBALVIEW-CH4 (2009) is used as a proxy for transport error, which largely dominates the observation error.

Methyl chloroform (MCF) is a molecule used in the past as an industrial solvent. Its use and emission have been restricted since the Montreal Protocol so that its concentration has exponentially decreased in the last decades. Following Montzka et al. (2000, 2011), only flask data from the NOAA network are used in our inversions. 12 sites have been selected over our study period; they are not homogeneously distributed (Fig. 1). During the inversion process, OH columns are scaled into 4 latitude bands to fit the MCF observations. At least one site with regular measurements is needed in each latitude band (see Sect. 2.1) to constrain the OH columns there. The regularity in the time-series is very important to constrain the loss of CH_4 over all the period. In the Southern tropical band, only Samoa Observatory (SMO) directly constrains the OH columns. SMO did not have a regular sampling; indeed this site does not record the MCF dry air mole fraction between April and July 2010. This implies that the chemical loss is not well constrained in this band. For MCF, we use the monthly variances averaged over each year from the Advanced Global Atmospheric Gases Experiment (AGAGE) program (Prinn et al., 2005) when available, otherwise from the NOAA. The averages, representing the synoptic variability, are used as observation errors.

3.3 Satellite observations

SCIAMACHY was operated onboard the European satellite ENVISAT between March 2002 and April 2012. It orbited at 800 km and covered the Earth in full every 6 days with a swath of 960 km and a ground resolution of 30 km (along track) and 60 km (across track) at nadir. The instrument observed the solar radiation reflected at the surface and the top of the atmosphere in the Short Wave Infra Red (SWIR) domain that allows deducing total columns of methane in cloud-free and sunlight conditions. The ratio of the CH_4 and CO_2 dry air mole fractions is retrieved together with the corresponding averaging kernels using the Iterative Maximum A Posteriori (IMAPv55) DOAS algorithm

ACPD
13, 8023–8064, 2013

detailed by Frankenberg et al. (2006). We use this ratio and the 4-D CO_2 analysis of Chevallier et al. (2011) to obtain the column-averaged dry air mole fraction of CH_4 (XCH_4). The retrievals have a lower accuracy at high latitudes and over the oceans, because the reflection of the solar radiation is very weak there. To avoid biases that may be introduced by these data and following Bergamaschi et al. (2009), we limit our study to the observations over land within 50° from the Equator and for which ground altitudes and model orography differ by less than 250 m. The selected XCH_4 data (Fig. 2a) are then averaged (non-weighted by their errors) into grid cells for each time step of the model so that "super-observations" are obtained. The uncertainty of the XCH_4 retrievals is around 2 % (Frankenberg et al., 2006). Following Spahni et al. (2011), a CTM error of 8 % of the observation values describing the inability of the model to represent the observations, is quadratically added to this retrieval error. In Sect. 4.3, an additional tuning will be computed based on the objective diagnostics described in Sect. 2.3: a multiplicative factor γ is estimated so that the new covariance matrix of the observation errors $\gamma\mathbf{R}$ satisfies Eqs. (6) and (7).

The Japanese satellite GOSAT was launched in January 2009 and has a polar sun-synchronous orbit at 667 km. It provides a full coverage of the Earth every 3 days with a swath of 750 km and a ground pixel resolution of 10.5 km at nadir. The TANSO-FTS instrument also observes in the SWIR domain. Version 3.2 of the TANSO-FTS XCH_4 proxy retrievals performed at the University of Leicester (Parker et al., 2011) are used with associated averaging kernels and a priori profiles. The XCH_4 retrieval algorithm uses an iterative retrieval scheme based on Bayesian optimal estimation. The retrieval accuracy is estimated to be about 0.6 %. CO_2 columns at appropriate time and location from Chevallier et al. (2011) are then used as a proxy for light path to retrieve the averaged mixing ratio of methane. A CTM error of 8 % of the observation is quadratically added to this error (see previous paragraph). Given the similarity between SCIAMACHY and TANSO-FTS measurements, we apply the data selection of the previous paragraph (see Fig. 2b) and create "super-observations" as well. Moreover, the

ACPD
13, 8023–8064, 2013

covariance matrix for TANSO-FTS **R** will also be tuned with a multiplicative scalar γ in Sect. 4.3.

The European MetOp-A satellite was launched in October 2006 and has a polar sun-synchronous orbit at an altitude of 817 km. Onboard MetOp-A, the Infrared Atmospheric Sounding Interferometer (IASI) measures the thermal radiation coming from the Earth and the atmosphere in the Thermal InfraRed domain (TIR) with a spectral resolution of 0.5 cm^{-1} apodized. It provides a full coverage every day with a swath of 1066 km and a ground resolution of 12 km at nadir. The retrieval algorithm is based on a non-linear inference scheme based on neural networks (Crevoisier et al., 2009, 2012). It allows inferring mid-to-upper troposphere columns of methane for the tropical band between 30° S and 30° N, including both land and ocean, twice a day at 09:30 a.m./p.m. local time, with an accuracy of 1.2 %. As IASI is not sensitive to CH_4 near the surface, it provides more accurate retrievals but covering less of the columns with a lower variability than TANSO-FTS and SCIAMACHY. A CTM error of 3 % of the CH_4 mid- to upper-troposphere columns is quadratically added to the retrieval error. Additional tuning of the observation error covariance matrix for IASI is done like for the other instruments in Sect. 4.3.2. This product (Fig. 2c) is used here without any quality control specific to this study but "super-observations" are created as well.

4 Results

4.1 Initial configurations

A series of grid-point inversions covering the period from June 2009 to December 2010 have been computed with the inverse model presented in Sect. 2 and the datasets presented in Sect. 3. To avoid edge effects, we study the methane emissions for the one-year period from August 2009 to July 2010. Posterior states given by the inversions are then aggregated at global or regional scales and evaluated at the local scale, i.e. at the surface sites. Each inversion will be called XX_γ^α with XX a two letter code specific to

ACPD
13, 8023–8064, 2013

each observing system (SC for SCIAMACHY, TA for TANSO-FTS, IA for IASI and SU for surface sites), α and γ the multiplicative factors associated, respectively, with the covariance matrices **B** (see Sect. 3.1) and **R** (see Sect. 3.3).

4.1.1 Global and regional budgets

Figure 3a presents the methane global annual emissions as inferred by the inversions. The global emission budgets of TANSO-FTS (TA_1^1) and SCIAMACHY (SC_1^1) are respectively increased by 3.9 % (+21 $Tg\,yr^{-1}$) and 4.2 % (+23 $Tg\,yr^{-1}$). They are decreased for IASI (IA_1^1) and the surface (SU_1^1) respectively by 4.3 % (−24 $Tg\,yr^{-1}$) and 3.6 % (−20 $Tg\,yr^{-1}$) when compared to the prior fluxes. Chemical losses, mostly constrained by MCF dry air mole fractions observed by surface sites (see Sect. 2.4), are increased by 0.4 % (+2 $Tg\,yr^{-1}$) for TA_1^1 only. For all the other observing systems, they are decreased by 1.4 % (−8 $Tg\,yr^{-1}$), 1.1 % (−6 $Tg\,yr^{-1}$) and 3 % (−16 $Tg\,yr^{-1}$) respectively for SC_1^1, IA_1^1 and SU_1^1. This leads to global annual growth rates of +39 $Tg\,yr^{-1}$, +51 $Tg\,yr^{-1}$, +2 $Tg\,yr^{-1}$ and +17 $Tg\,yr^{-1}$ respectively for TA_1^1, SC_1^1, IA_1^1 and SU_1^1. Uncertainty reductions on global budgets, estimated with a Monte-Carlo approach as detailed in Sect. 2.1, are of 42 %, 51 %, 62 % and 60 % respectively for TA_1^1, SC_1^1, IA_1^1 and SU_1^1. Global posterior uncertainties are inferred from uncertainty reduction and global prior uncertainties of 53 $Tg\,yr^{-1}$ to complete the description of posterior global annual estimates of methane. The global emission budgets amount to 577 ± 31 $Tg\,yr^{-1}$, 578 ± 26 $Tg\,yr^{-1}$, 531 ± 20 $Tg\,yr^{-1}$ and 535 ± 21 $Tg\,yr^{-1}$ respectively for TA_1^1, SC_1^1, IA_1^1 and SU_1^1. As shown by Fig. 3a, with error bars representing the 1-sigma standard deviations, the global emissions and chemical losses of methane inferred from the different observing systems are statistically consistent with each other.

The methane emissions are then aggregated over large continental regions (shown in Fig. 4a and adapted from Gurney et al., 2002). As shown by Fig. 4b, the three satellites show a very good agreement for 6 regions: North American Boreal, USA, South American Temperate, Eurasian Boreal, South Asia and Australia. This agreement may

ACPD
13, 8023–8064, 2013

reflect a good improvement on methane emissions, consistent from one satellite to another, where we find large uncertainty reductions like in regions South American Temperate (39 %, 42 % and 55 % of uncertainty reduction for respectively SC_1^1, TA_1^1 and IA_1^1) and South Asia (44 %, 34 % and 51 % of uncertainty reduction for respectively SC_1^1, TA_1^1 and IA_1^1). This agreement may also reflect no real improvement on methane emissions that stay close to the prior, where the uncertainty reductions are very weak, like in regions North American Boreal (1 %, 8 % and 4 % of uncertainty reduction for respectively SC_1^1, TA_1^1 and IA_1^1) and Australia (2 %, 2 % and 8 % of uncertainty reduction for respectively SC_1^1, TA_1^1 and IA_1^1). However, large differences are found between satellite and surface inversions for regions USA (14 %, 19 %, 16 % and 34 % of uncertainty reduction for respectively SC_1^1, TA_1^1, IA_1^1 and SU_1^1), South American Temperate (39 %, 42 %, 55 % and 32 % of uncertainty reduction for respectively SC_1^1, TA_1^1, IA_1^1 and SU_1^1), South Asia (44 %, 34 %, 51 % and 31 % of uncertainty reduction for respectively SC_1^1, TA_1^1, IA_1^1 and SU_1^1) and South East Asia (35 %, 42 %, 51 % and 55 % of uncertainty reduction for respectively SC_1^1, TA_1^1, IA_1^1 and SU_1^1). The surface does not agree with the satellites especially in the Tropics where there are few surface observational sites. Large differences between IASI and the other observing systems are also found in regions Southern Africa (12 %, 15 %, 32 % and 27 % of uncertainty reduction for respectively SC_1^1, TA_1^1, IA_1^1 and SU_1^1), South East Asia (35 %, 42 %, 51 % and 52 % of uncertainty reduction for respectively SC_1^1, TA_1^1, IA_1^1 and SU_1^1) and Indonesia (18 %, 30 %, 63 % and 38 % of uncertainty reduction for respectively SC_1^1, TA_1^1, IA_1^1 and SU_1^1). Although IASI has a dense spatial coverage, we found inconsistencies with the other observing systems in regions South East Asia and Indonesia. This may be due to a misattribution of the emissions in these regions because of a lack of data during the monsoon period.

ACPD
13, 8023–8064, 2013

4.1.2 Initial conditions

2-D scaling factors adjust the initial conditions of CH_4 and MCF on 1 June 2009 at 00:00 UTC (see Sect. 2.4) and therefore affect the mass budget of the inversion. After the inversions SC_1^1, TA_1^1 and IA_1^1, the initial CH_4 columns show increments of about $1.1 \pm 0.6\,\%$, $0.3 \pm 0.6\,\%$ and $0.4 \pm 0.9\,\%$ respectively. The spatial distribution of these columns is very different between SCIAMACHY and the other two satellites. Figure 5b shows a decrease of the amplitude of the columns in the two hemispheres that can reach 3 % for SCIAMACHY. However, for TANSO-FTS and IASI, Fig. 5a, b show an increase in the Southern Hemisphere, especially in the Tropics, that can reach 3 % for both instruments, and a slight decrease (respectively less than 1 % and less than 2 %) in the Northern Hemisphere.

4.1.3 Fit to surface measurements

The fit to the surface data is summarized by the mean bias (last column of Table 2) and the mean root mean square between the posterior states obtained by using the different satellite datasets, respectively TA_1^1, SC_1^1 and IA_1^1, and their equivalent seen at each independent surface site (see Fig. 6a–c, respectively). The mean bias obtained by TA_1^1 is 4.6 ppb which is 5 times smaller than the SC_1^1 one (26.9 ppb) and 3 times smaller than the IA_1^1 one (15.1 ppb). The mean root mean square obtained by TA_1^1 is 23.5 ppb, the one by SC_1^1 is 37.7 ppb and the one by IA_1^1 is 35.1 ppb. Only TANSO-FTS is able to produce a posterior state consistent with surface measurements whereas SCIAMACHY and IASI infer larger mean biases to surface sites.

4.2 Bias correction

A bias correction as a function of the airmass factor A_F (see Sect. 2.2) is applied on TANSO-FTS and SCIAMACHY retrievals as presented in Sect. 3.3. $SC_1^1C_{AF}$ and $TA_1^1C_{AF}$ represent the inversions using bias-corrected satellite retrievals of

ACPD
13, 8023–8064, 2013

SCIAMACHY and TANSO-FTS respectively. As shown by Fig. 7a, b, the linear model is $4.0 \times A_F - 34.0$ ppb for TANSO-FTS and $13.7 \times A_F - 26.6$ ppb for SCIAMACHY. $SC_1^1C_{AF}$ and $TA_1^1C_{AF}$ are respectively compared to SC_1^1 and TA_1^1 of Sect. 4.1 to evaluate the impact of such a correction.

4.2.1 Global and regional budgets

At the global scale, as shown by Fig. 3b, the bias correction decreases both posterior emissions and losses for TANSO-FTS respectively by 1 % (6 $Tg\,yr^{-1}$) and 0.6 % (3 $Tg\,yr^{-1}$) leading to a decrease of 7 % of the annual growth rate (36 $Tg\,yr^{-1}$ instead of 39 $Tg\,yr^{-1}$ without correction). For SCIAMACHY, the correction increases both posterior emissions and losses respectively by 4 % (25 $Tg\,yr^{-1}$) and 3 % (15 $Tg\,yr^{-1}$), leading to an increase of the annual growth rate of 20 % (61 $Tg\,yr^{-1}$ instead of 51 $Tg\,yr^{-1}$ without correction). The correction induces larger increments for SCIAMACHY chemical losses, which are 5 times larger than for TANSO-FTS. This highlights the fact that chemical losses are not only driven by MCF observations in this inversion system, but also by CH_4 observations. When compared to the reference SU_1^1, TANSO-FTS shows an annual growth rate closer to the surface data when using the bias correction, but this is not the case for SCIAMACHY, due to the larger regression slope for this instrument (see Fig. 7a), combined with the seasonal cycle of the data coverage (see Sect. 2.2).

We now study the impact of the bias correction at the regional scale. When compared to the non-corrected inversion TA_1^1, posterior methane emissions of $TA_1^1C_{AF}$ are slightly increased or decreased getting closer to the reference inversion for all regions. As shown by Fig. 4c, the emissions are increased especially in mid- and high-latitudes, like in region East Europe (+34 %). They are decreased especially in the Tropics, like in region Indonesia (−7.6 %). For SCIAMACHY, the correction infers large increases or decreases consistent with the reference increments for almost all regions with exceptions particularly in regions South American tropical (+22 %), South American Temperate (3 %) and Indonesia (+25 %), three regions accounting for one third of the global methane emissions. As surface measurements are especially located in mid- and high-

ACPD
13, 8023–8064, 2013

latitudes, it makes sense that the largest inconsistencies with the reference concern the Tropics.

4.2.2 Initial conditions

Whereas better agreement is shown between TANSO-FTS and the surface, SCIAMACHY cannot be reconciled with the reference at global and regional scales. The larger emissions and losses of $SC_1^1C_{AF}$ illustrates the fact that the analysis state may also depend on the initial conditions. In fact, the CH_4 initial columns vary by $1.1 \pm 0.6\,\%$ without correction (SC_1^1) and by $0.8 \pm 1.3\,\%$ with the bias correction ($SC_1^1C_{AF}$) inducing larger variations spread all over the globe for the corrected version. As shown by Fig. 5e, the largest positive variations are located in the tropical part of the Southern Hemisphere and can locally reach 5 %. However, this makes the spatial distribution of the $SC_1^1C_{AF}$ initial conditions more consistent with TA_1^1 or $TA_1^1C_{AF}$ initial conditions (Fig. 5a, d).

4.2.3 Fit to surface measurements

For TANSO-FTS, the mean bias between the model and the surface observations is reduced from 4.6 ppb to 1.2 ppb (see Table 2) and the mean root mean square is slightly reduced from 23.5 ppb to 22.8 ppb after the bias correction. The bias correction improves the fit to surface sites, especially in the Northern Hemisphere where five more sites show better agreement between surface measurements and the posterior state of the corrected version $TA_1^1C_{AF}$ (Fig. 6e). For SCIAMACHY, the fit to the surface sites is also better (Fig. 6e). The bias correction improves the fit for 10 sites located in the two hemispheres while the mean bias is significantly reduced from 26.9 ppb to 4.7 ppb and the mean root mean square reduced from 37.7 ppb to 30.4 ppb, now comparable to TANSO-FTS without any correction.

ACPD
13, 8023–8064, 2013

4.3 Diagnostics on prior, observations and analysis variances

4.3.1 Tuning prior error variances

The diagnostics applied on the inversion SU_1^1 shows that the observation error variances for the surface measurements are fairly represented in the inversion system ($ratio_o = 0.92$, with $ratio_o = \frac{diag_o}{var_o}$ as defined in Sect. 2.3), while prior error variances are over-estimated by a two-fold factor ($ratio_b = 2.02$). We use the diagnostics of this inversion to tune the prior error variances. Table 3 presents the results for the inversion $SU_1^{0.6}$ using surface measurements and $\alpha = 0.6$ for prior errors. Diagnostics now show better ratios for both observation and prior error variances ($ratio_o = 0.97$ and $ratio_b = 1.05$). To simplify the comparison between the inversions using the different observing systems, we set $\alpha = 0.6$ for prior errors of all the inversions and $SU_1^{0.6}$ is taken as the reference from now on. The diagnostics of the inversions using this new configuration for prior errors are presented in Table 3. The tuning of the prior errors improves the analysis variances for $TA_1^{0.6}$, $SC_1^{0.6}$ and $IA_1^{0.6}$ (respectively $ratio_a = 1.07$, $ratio_a = 1.07$ and $ratio_a = 0.28$ instead of respectively $ratio_a = 0.71$, $ratio_a = 0.66$ and $ratio_a = 2.47$ for TA_1^1, SC_1^1 and IA_1^1). Otherwise, this tuning degrades the diagnostics of prior error variances for SCIAMACHY and TANSO-FTS (respectively $ratio_b = 0.49$ and $ratio_b = 0.63$ instead of respectively $ratio_b = 0.72$ and $ratio_b = 0.99$) suggesting that the variance estimation process does not converge in this case; we remind that only one iteration is computed for these diagnostics (see Sect. 2.3).

4.3.2 Tuning observation error variances

Several configuration tests are computed to tune observation error variances from Eq. (6). As presented in Table 3, the diagnostics show an over-estimation of the observation error variances for the three satellites $TA_1^{0.6}$, $SC_1^{0.6}$ and $IA_1^{0.6}$. These errors seem to be over-estimated by a 9-fold factor for TANSO-FTS ($ratio_o = 9.23$), by a 5-fold factor for SCIAMACHY ($ratio_o = 4.62$) and by a 4-fold factor for IASI ($ratio_o = 4.01$).

ACPD
13, 8023–8064, 2013

Some tests are computed by reducing the model component of the observation errors. A good improvement of observation error variances is shown for $TA^{0.6}_{0.075}$ ($ratio_o$ = 1.21) and $SC^{0.6}_{0.175}$ ($ratio_o$ = 0.99). Observation error variances are also improved for $IA^{0.6}_{0.33}$ ($ratio_o$ = 0.27). Comparing inversions TA^{1}_{1} and $TA^{0.6}_{0.075}$ shows that observation error variances can be improved, i.e. $ratio_o$ is reduced from 8.9 to 1.21, whereas the analysis error variances are degraded, i.e. with $ratio_a$ increased from 1.07 to 1.55. We link the initial value of $ratio_o$ with our use of a diagonal **R**, with inflated variances qualitatively compensating for missing correlations (see Sect. 2.1). The diagnostics do not account for this numerical artifact. By tuning the observation error variances with the ratio obtained from the diagnostics on the analysis variances, i.e. from Eq. (4) rather than Eq. (6), (see Sect. 2.3), the inversion $TA^{0.6}_{0.125}$ shows an improved analysis ratio ($ratio_a$ = 1.11) but we do not find better configurations for SCIAMACHY and IASI than $SC^{0.6}_{0.2}$ and $IA^{0.6}_{0.33}$.

4.4 Final configurations

The most statistically-consistent inversions according to the diagnostics on variances are configurations $TA^{0.6}_{0.125}$, $SC^{0.6}_{0.2}$ and $IA^{0.6}_{0.33}$. In the following, posterior methane emissions and losses from these three configurations are presented at global and regional scales and evaluated at surface sites.

4.4.1 Global and regional budgets

For the inversions $TA^{0.6}_{0.125}$, $SC^{0.6}_{0.2}$ and $IA^{0.6}_{0.33}$, the global posterior emissions are respectively 567 $Tg\,yr^{-1}$, 608 $Tg\,yr^{-1}$ and 524 $Tg\,yr^{-1}$ and the global losses are respectively 545 $Tg\,yr^{-1}$, 548 $Tg\,yr^{-1}$ and 524 $Tg\,yr^{-1}$ (Fig. 3c). This leads to global growth rates of respectively +27 $Tg\,yr^{-1}$, +60 $Tg\,yr^{-1}$ and 0 $Tg\,yr^{-1}$. Only TANSO-FTS retrieves a growth rate consistent with $SU^{0.6}_{1}$. The posterior growth rate of $IA^{0.6}_{0.33}$ is close to 0 $Tg\,yr^{-1}$. However, the tropical growth rates (within 30° from the Equator) of IASI and

ACPD
13, 8023–8064, 2013

the surface are in very good agreement, respectively $-54\,\mathrm{Tg\,yr^{-1}}$ and $-52\,\mathrm{Tg\,yr^{-1}}$ instead of respectively $-33\,\mathrm{Tg\,yr^{-1}}$ and $-62\,\mathrm{Tg\,yr^{-1}}$ for the initial configurations IA_1^1 and SU_1^1. SCIAMACHY over-estimates the growth rate by as much as 4-fold when compared to $SU_1^{0.6}$ and 2-fold when compared to $TA_{0.125}^{0.6}$. Even when increasing the observation error variances to account for the missing correlations between the observations and the bias identified in Sect. 2.2, the growth rate inferred by SCIAMACHY remains too high meaning that the instrument is more difficult to exploit.

At the regional scale , when comparing the final configurations (Fig. 4d) with the initial configurations (Fig. 4b), the observing systems still show a good agreement for regions North American Boreal, Eurasian Boreal and Australia and show better consistency for regions USA, Northern Africa, Southern Africa, West Europe and Middle East. Differences are found for regions South American tropical and East Europe where TANSO-FTS does not agree with the other two observing systems. Differences between IASI and the others are also found in regions South American Temperate, South Asia, South East Asia and Indonesia. As for the initial configurations, there is probably a misattribution of the emissions in these regions due to a lack of data during the monsoon period. However, the large differences found in the initial configurations are reduced for these new configurations suggesting that improving the statistical consistency in our system improves the consistency between the different observing systems in terms of emissions.

4.4.2 Initial conditions

As shown by Fig. 5f–h, the CH_4 initial columns show variations of $0.1\% \pm 1.2\%$ for inversion $TA_1^{0.6}$, $1.6\% \pm 2\%$ for $SC_{0.2}^{0.6}$, $0.4 \pm 0.9\%$ for $IA_{0.33}^{0.6}$ with the largest variations mostly located in the tropical part of the Southern Hemisphere reaching respectively 5 %, 6 % and 3 % instead of 3 % for the three initial configurations of the satellite instruments. This highlights that the statistical consistency can also have an important

ACPD
13, 8023–8064, 2013

impact on the adjustment of the initial conditions; they vary by 2-fold for SCIAMACHY. Moreover, $SC^{0.6}_{0.2}$ and SC^{1}_{1} initial conditions have very different spatial distributions.

4.4.3 Fit to surface measurements

The mean bias to the surface measurements is the largest when using SCIAMACHY observations (38.2 ppb) and the mean root mean square is about 51.1 ppb. The most statistically-consistent configuration for TANSO-FTS according to the observation diagnostics, $TA^{0.6}_{0.125}$, has a growth rate of 27 $Tg\,yr^{-1}$ consistent with the surface but not the smallest mean bias-based estimation (4.6 ppb) (see Fig. 6f) and a mean root mean square of 24 ppb. The mean bias to the surface measurements is 7.7 ppb for IASI (Fig. 6g), which is now comparable to the TANSO-FTS one, and the mean root mean square is about 26.1 ppb. Refining the statistical consistency of our system improves the fit to surface measurements for TANSO-FTS and IASI, but not for SCIAMACHY.

4.5 Combination of TANSO-FTS and surface observations

We finally test a combination of TANSO-FTS and of CH_4 surface measurements at high latitudes (i.e. over 50° N and 50° S only) where no satellite data are assimilated (see Sect. 3.3). We use the TANSO-FTS observations with the $TA^{0.6}_{0.075}$ configuration and the $SU^{0.6}_{1}$ configuration for surface measurements.

4.5.1 Global and regional budgets

As shown by Fig. 3d, no large differences on global emissions are found when using surface sites coupled with TANSO-FTS or when using TANSO-FTS alone. The global emissions are almost the same for $TA^{0.6}_{0.075}$ and $TASU^{0.6}_{0.075}$ (respectively 567 $Tg\,yr^{-1}$ and 566 $Tg\,yr^{-1}$) but there is a larger difference for global losses (respectively 543 $Tg\,yr^{-1}$ and 538 $Tg\,yr^{-1}$), meaning that CH_4 measurements play also a significant role to estimate the methane chemical loss. Adding the surface sites outside the domain

ACPD
13, 8023–8064, 2013

50° S–50° N increases the global growth rate by 36 %, i.e. from 17 Tg yr^{-1} ($TA^{0.6}_{0.075}$) to 24 Tg yr^{-1} ($TASU^{0.6}_{0.075}$) whereas the inversion using surface measurements only has a growth rate of 18 Tg yr^{-1} which is closer to $TA^{0.6}_{0.075}$.

At the regional scale, as shown by Fig. 4e, adding the surface sites at high latitudes leads to an emission increase consistent with $SU^{0.6}_{1}$ in regions North American Boreal (41 % corresponding to 5.4 Tg yr^{-1}), Eurasian Boreal (65 %, 7.3 Tg yr^{-1}) and East Europe (49 %, 7.3 Tg yr^{-1}). It also decreases emissions consistent with $SU^{0.6}_{1}$ in regions South American tropical (3.7 %, −2 Tg yr^{-1}), South American Temperate (15 %, −10 Tg yr^{-1}), West Europe (18.5 %, −5.2 Tg yr^{-1}), South Asia (11 %, −7 Tg yr^{-1}) and South East Asia (5 %, −4.3 Tg yr^{-1}). The largest differences between $TA^{0.6}_{0.075}$ and $TASU^{0.6}_{0.075}$ that do not agree with $SU^{0.6}_{1}$ concern the regions USA (−20 %, i.e. −8 Tg yr^{-1}), South American Temperate (−15 %, −10 Tg yr^{-1}) and Indonesia (−35 %, +16 Tg yr^{-1}). The global emissions do not vary by adding surface sites at high latitudes but the spatial distribution of these emissions may be very different.

4.5.2 Initial conditions

The CH_4 columns are slightly different than for $TA^{0.6}_{0.075}$ with a variation of 0.8 ± 1.2 % for $TA^{0.6}_{0.075}$ and 0.5 ± 1.2 % for $TASU^{0.6}_{0.075}$. The spatial distributions are almost the same as well. The highest variations are located in the tropical part of the Southern Hemisphere reaching 4 % (see Fig. 5i, j). However, there are weaker variations of the initial conditions in the Northern Hemisphere for $TASU^{0.6}_{0.075}$, especially at high latitudes, which are more constrained by CH_4 surface sites.

4.5.3 Fit to surface measurements

The global mean biases and mean root mean square quantified at $TASU^{0.6}_{0.075}$-independent sites (i.e. within 50° from the Equator) are 2.4 ppb and 20.8 ppb for $TA^{0.6}_{0.075}$

ACPD
13, 8023–8064, 2013

(Fig. 6h) and 0.2 ppb and 21.3 ppb for $TASU^{0.6}_{0.075}$ (Fig. 6i) while they are 2.2 ppb and 10.7 ppb for $TA^{0.6}_{0.075}$ and 0.4 ppb and 5.4 ppb for $TASU^{0.6}_{0.075}$ when quantified at $TASU^{0.6}_{0.075}$-dependent sites. The global mean biases are almost 10 times smaller when using surface measurements at high latitudes and are the smallest of all tests.

5 Discussion

The two satellite instruments observing in the SWIR domain, TANSO-FTS and SCIAMACHY, infer larger emissions, respectively by $+41\,Tg\,yr^{-1}$ and $+43\,Tg\,yr^{-1}$, when compared to the reference global budget of $526\,Tg\,yr^{-1}$. This over-estimation can be partly explained by a bias identified as a function of the airmass factor in the satellite products, respectively of $4.0 \times A_F - 34.0$ ppb and $14.7 \times A_F - 26.6$ ppb. Correcting this bias improves the agreement between TANSO-FTS and the reference at global and regional scales and the fit to surface measurements as well. However, given the modesty of the bias and the uncertainty of the linear regression, its need is not obvious. For SCIAMACHY, the impact of the bias correction on the inverted methane emissions is larger but such a correction does not improve the agreement with the reference at global and regional scales in terms of emissions, while it improves the fit to the surface measurements in terms of mole fractions. Such a correction is needed for SCIAMACHY but not sufficient to reconcile the methane emissions and losses with those of the reference.

Following their heterogeneous distribution, surface sites observing MCF mainly drive the inverted loss in the Southern Hemisphere. The variations of 2-D OH concentrations can reach 22 % in the tropical part of the Southern Hemisphere for $TA^{0.6}_{0.075}$. In fact, the loss of methane in the band $-30^{\circ}/0^{\circ}$ is less constrained. Only one site observing MCF concentrations is localized in this band, the time series of which is unfortunately not regular, with missing values between April and July 2010 (Sect. 3.2). However, the variations of the OH columns are not so large for all cases and are less than 2 standard

ACPD
13, 8023–8064, 2013

deviations for inversions $TA^{0.6}_{0.125}$, $IA^{0.6}_{0.33}$ and $SU^{0.6}_{1}$; the losses of methane are not much affected in these cases.

The inverted methane emissions depend on the representation of the error statistics in our system to a larger extent. Several iterations of the variance diagnostics in the observation space allow improving the statistical consistency and the agreement with the reference. In fact, the most statistically-consistent inversion using TANSO-FTS measurements, $TA^{0.6}_{0.125}$, shows better agreement to the surface inversion and a remarkably good fit to surface sites (4.8 ppb of standard deviation). For SCIAMACHY, all the sensitivity tests show better fit to surface sites whereas the methane emissions are still too large when compared to the reference. It seems that SCIAMACHY cannot agree with the reference by simply adjusting mean prior and observation error variances. This points to a complicated structure of the retrieval errors, at least for the period studied, possibly linked to the progressive degradation of the instrument.

The diagnostics improve the consistency between the inverted methane emissions inferred from the different observing systems. In fact, the posterior states of $TA^{0.6}_{0.125}$, $IA^{0.6}_{0.33}$ and $SU^{0.6}_{1}$ have similar methane emission spatial distributions. For all observing systems, the highest emissions are in region South American tropical and may be explained by biomass burning further to the severe drought in Amazonia in 2010. Large emissions are inferred as well in region South Africa, which are probably due to biomass burning. By comparing the posterior emissions with a study of Bouwman et al. (1993), we can see a good correspondence between soil drainage and methane emissions in boreal regions (region North American Boreal and the west part of region Eurasian Boreal) but also in regions South Asia and South East Asia probably linked to the cultivation of rice. IASI differs from the other two observing systems in some regions: an over-estimation of the emissions (when compared to the reference) in Indonesia compensates an under-estimation of the emissions in India showing a misattribution of the emissions in these regions likely because clouds during the monsoon period, i.e. between June and September, prevent the retrieval. Another under-estimation of the emissions in region South American tropical is seen as well due to a lack of

ACPD
13, 8023–8064, 2013

IASI retrievals over this region between November 2009 and March 2010. This does not allow inverting the high emissions observed by TANSO-FTS and the surface data during the drought of 2010.

The three observing systems still show good consistency in terms of emissions, meaning we can trust the main information retrieved from the different observing systems, apart from SCIAMACHY, and can properly combine them together. A combination of TANSO-FTS and of the surface sites at high latitudes, i.e. where no satellite observations have a sufficient accuracy, improves the fit to surface sites especially in the Northern Hemisphere even for sites that are not used in the inversion. However, in the Southern Hemisphere the fit is not improved for the sites optimized during the inversion. Interestingly, we found a similar problem when inverting CO emissions from the Measurements Of Pollution In The Troposphere (MOPITT) onboard NASA's Terra satellite (Fortems-Cheiney et al., 2011). These two results may be partly explained by the too small time exchange of the model LMDz from the Northern Hemisphere to the Southern Hemisphere as shown by a study of Patra et al. (2011) which likely induces an artificial increase of the sources inferred in the North and an increase of the loss in the South to match the surface observations. This can also be amplified by the lack of constraint for OH in the tropical part of the Southern Hemisphere.

6 Conclusion

Our study highlights the need of statistical consistency in variational data assimilation systems. We show that, by using objective tuning methods for the error statistics, we can reconcile different observing systems, with the exception of SCIAMACHY which seems to be particularly difficult to exploit over the period 2009–2010. These diagnostics have a larger impact on methane emissions and chemical losses at global and regional scales than a bias correction directly on the satellite products. The tuning reduces the global annual prior error from 53 $\mathrm{Tg\,yr^{-1}}$ to 36 $\mathrm{Tg\,yr^{-1}}$ ($\alpha = 0.6$). The tuned covariance matrix is more optimistic than our initial conservative estimate. The

ACPD
13, 8023–8064, 2013

observation model error, initially set at 8 % for TANSO-FTS and SCIAMACHY and 3 % for IASI, is reduced by a multiplicative factor $\gamma = 0.125$ for TANSO-FTS, $\gamma = 0.175$ for SCIAMACHY and $\gamma = 0.33$ for IASI. The global TANSO-FTS, IASI and surface data budgets from the improved configurations are $568 \pm 17\,\mathrm{Tg\,yr^{-1}}$, 524 ± 16 and $538 \pm 20\,\mathrm{Tg\,yr^{-1}}$. By improving the statistical consistency of the inversion system, we can reconcile data from current satellites and data from the surface. We can then keep one of the available datasets out of the inversion for independent evaluation. Alternatively, we can combine them together to best reduce the uncertainty about methane emissions.

Acknowledgements. The first author is funded by CNES and CEA. This work was performed using HPC resources from DSM-CCRT and [CCRT/CINES/IDRIS] under the allocation 2012-t2012012201 made by GENCI (Grand Equipement National de Calcul Intensif). We also thank the computing support team of the LSCE led by F. Marabelle. We aknowledge the contributors to the World Data Center for Greenhouse Gases for providing their data of methane and methyl-chloroform atmospheric mole fractions. The authors thank in particular S. Piacentino (ENEA), T. Kawasato (JMA) and S. Nichol (NIWA). NOAA authors receive partial funding for their measurements and research from the Atmospheric Chemistry, Carbon Cycle, and Climate (AC4) Program. The GOSAT XCH_4 was generated at the University of Leicester and funded as part of the ESA Climate Change Initiative.

The publication of this article is financed by CNRS-INSU.

ACPD
13, 8023–8064, 2013

References

Artuso, F., Chamard, P., Piacentino, S., Di Sarra, A., Meloni, D., Monteleone, F., Sferlazzo, D., and Thiery, F.: Atmospheric methane in the Mediterranean: analysis of measurements at the island of Lampedusa during 1995–2005, Atmos. Environ., 41, 3877–3888, 2007. 8032

Bergamaschi, P., Frankenberg, C., Meirink, J., Krol, M., Villani, M., Houweling, S., Dentener, F., Dlugokencky, E., Miller, J., Gatti, L., Engel, A., and Levin I.: Inverse modeling of global and regional CH4 emissions using SCIAMACHY satellite retrievals, J. Geophys. Res., 114, D22301, doi:10.1029/2009JD012287, 2009. 8029, 8034

Bocquet, M., Wu, L., and Chevallier, F.: Bayesian design of control space for optimal assimilation of observations. Part I: Consistent multiscale formalism, Q. J. Roy. Meteor. Soc., 137, 1340–1356, 2011. 8027

Bousquet, P., Hauglustaine, D. A., Peylin, P., Carouge, C., and Ciais, P.: Two decades of OH variability as inferred by an inversion of atmospheric transport and chemistry of methyl chloroform, Atmos. Chem. Phys., 5, 2635–2656, doi:10.5194/acp-5-2635-2005, 2005. 8032

Bousquet, P., Ringeval, B., Pison, I., Dlugokencky, E. J., Brunke, E.-G., Carouge, C., Chevallier, F., Fortems-Cheiney, A., Frankenberg, C., Hauglustaine, D. A., Krummel, P. B., Langenfelds, R. L., Ramonet, M., Schmidt, M., Steele, L. P., Szopa, S., Yver, C., Viovy, N., and Ciais, P.: Source attribution of the changes in atmospheric methane for 2006–2008, Atmos. Chem. Phys., 11, 3689–3700, doi:10.5194/acp-11-3689-2011, 2011. 8025

Bouwman, A., Fung, I., Matthews, E., and John, J.: Global analysis of the potential for N_2O production in natural soils, Global Biogeochem. Cy., 7, 557–597, 1993. 8047

Chapnik, B., Desroziers, G., Rabier, F., and Talagrand, O.: Diagnosis and tuning of observational error in a quasi-operational data assimilation setting, Q. J. Roy. Meteor. Soc., 132, 543–565, 2006. 8028

Chevallier, F.: Impact of correlated observation errors on inverted CO_2 surface fluxes from OCO measurements, Geophys. Res. Lett., 34, L24804, doi:10.1029/2007GL030463, 2007. 8028

Chevallier, F., Fisher, M., Peylin, P., Serrar, S., Bousquet, P., Breon, F., Chédin, A., and Ciais, P.: Inferring CO_2 sources and sinks from satellite observations: method and application to TOVS data, J. Geophys. Res, 110, D24309, doi:10.1029/2005JD006390, 2005. 8027

Chevallier, F., Bréon, F., and Rayner, P.: Contribution of the orbiting carbon observatory to the estimation of CO_2 sources and sinks: theoretical study in a variational data assimilation framework, J. Geophys. Res., 112, D09307, doi:10.1029/2006JD007375, 2007. 8028

ACPD
13, 8023–8064, 2013

Chevallier, F., Maksyutov, S., Bousquet, P., Bréon, F., Saito, R., Yoshida, Y., and Yokota, T.: On the impact of transport model errors for the estimation of CO_2 surface fluxes from GOSAT observations, Geophys. Res. Lett., 37, L21803, doi:10.1029/2010GL044652, 2011. 8034

Crevoisier, C., Nobileau, D., Fiore, A. M., Armante, R., Chédin, A., and Scott, N. A.: Tropospheric methane in the tropics – first year from IASI hyperspectral infrared observations, Atmos. Chem. Phys., 9, 6337–6350, doi:10.5194/acp-9-6337-2009, 2009. 8035

Crevoisier, C., Nobileau, D., Armante, R., Crépeau, L., Machida, T., Sawa, Y., Matsueda, H., Schuck, T., Thonat, T., Pernin, J., Scott, N. A., and Chédin, A.: The 2007–2011 evolution of tropical methane in the mid-troposphere as seen from space by MetOp-A/IASI, Atmos. Chem. Phys. Discuss., 12, 23731–23757, doi:10.5194/acpd-12-23731-2012, 2012. 8035

Desroziers, G., Berre, L., Chapnik, B., and Poli, P.: Diagnosis of observation, background and analysis-error statistics in observation space, Q. J. Roy. Meteor. Soc., 131, 3385–3396, 2006. 8030

Dlugokencky, E., Steele, L., Lang, P., and Masarie, K.: The growth rate and distribution of atmospheric methane, J. Geophys. Res., 99, 17–21, 1994. 8032

Dlugokencky, E., Bruhwiler, L., White, J., Emmons, L., Novelli, P., Montzka, S., Masarie, K., Lang, P., Crotwell, A., Miller, J., and Gatti, L. V.: Observational constraints on recent increases in the atmospheric CH_4 burden, Geophys. Res. Lett., 36, L18803, doi:10.1029/2009GL039780, 2009. 8032

Forster, P.: Changes in Atmospheric Constituents and in Radiative Forcing, Cambridge University Press, UK and New York, NY, USA, 2007. 8025

Fortems-Cheiney, A., Chevallier, F., Pison, I., Bousquet, P., Szopa, S., Deeter, M., and Clerbaux, C.: Ten years of CO emissions as seen from Measurements of Pollution in the Troposphere (MOPITT), J. Geophys. Res., 116, D05304, doi:10.1029/2010JD014416, 2011. 8048

Francey, R., Steele, L., Langenfelds, R., and Pak, B.: High precision long-term monitoring of radiatively active and related trace gases at surface sites and from aircraft in the Southern Hemisphere atmosphere, J. Atmos. Sci., 56, 279–285, 1999. 8033

Frankenberg, C., Meirink, J., Bergamaschi, P., Goede, A., Heimann, M., Körner, S., Platt, U., Van Weele, M., and Wagner, T.: Satellite chartography of atmospheric methane from SCIAMACHY on board ENVISAT: analysis of the years 2003 and 2004, J. Geophys. Res., 111, D07303, doi:10.1029/2005JD006235, 2006. 8034

Gilbert, J. and Lemaréchal, C.: Some numerical experiments with variable-storage quasi-Newton algorithms, Math. Program., 45, 407–435, 1989. 8028

ACPD
13, 8023–8064, 2013

GLOBALVIEW-CH4: Cooperative Atmospheric Data Integration Project – Methane, CD-ROM, NOAA ESRL, Boulder, Colorado, 2009. 8033

Gurney, K., Law, R., Denning, A., Rayner, P., Baker, D., Bousquet, P., Bruhwiler, L., Chen, Y., Ciais, P., Fan, S., Fung, I. Y., Gloor, M., Heimann, M., Higuchi, H., John, J., Maki, T., Maksyutov, S., Masarie, K., Peylin, P., Prather, M., Pak, B. C., Randerson, J., Sarmiento, J., Taguchi, S., Takahashi, T., and Yuen, C. W.: Towards robust regional estimates of CO_2 sources and sinks using atmospheric transport models, Nature, 415, 626–630, doi:10.1038/415626a, 2002. 8036

Hauglustaine, D., Hourdin, F., Jourdain, L., Filiberti, M., Walters, S., Lamarque, J., and Holland, E.: Interactive chemistry in the Laboratoire de Météorologie Dynamique general circulation model: description and background tropospheric chemistry evaluation, J. Geophys. Res, 109, 4314–4357, 2004. 8031

Hourdin, F., Musat, I., Bony, S., Braconnot, P., Codron, F., Dufresne, J., Fairhead, L., Filiberti, M., Friedlingstein, P., Grandpeix, J., Krinner, G., LeVan, P., Li, Z. X., and Lott, F.: The LMDZ4 general circulation model: climate performance and sensitivity to parametrized physics with emphasis on tropical convection, Clim. Dynam., 27, 787–813, doi:10.1007/s00382-006-0158-0, 2006. 8031

Kaminski, T., Rayner, P., Heimann, M., and Enting, I.: On aggregation errors in atmospheric transport inversions, J. Geophys. Res., 105, 4703–4715, 2001. 8027

Kaplan, J.: Wetlands at the last glacial maximum: distribution and methane emissions, Geophys. Res. Lett., 29, 1079, doi:10.1029/2001GL013366, 2002. 8031, 8055

Lambert, G. and Schmidt, S.: Reevaluation of the oceanic flux of methane: uncertainties and long term variations, Chemosphere, 26, 579–589, 1993. 8031, 8055

Lowe, D., Brenninkmeijer, C., Tyler, S., and Dlugkencky, E.: Determination of the isotopic composition of atmospheric methane and its application in the Antarctic, J. Geophys. Res., 96, 15455–15467, 1991. 8033

Matsueda, H., Sawa, Y., Wada, A., Inoue, H., Suda, K., Hirano, Y., Tsuboi, K., and Nishioka, S.: Methane standard gases for atmospheric measurements at the MRI and JMA and intercomparison experiments, Pap. Meteorol. Geophys., 54, 91–113, 2004. 8032

Montzka, S., Spivakovsky, C., Butler, J., Elkins, J., Lock, L., and Mondeel, D.: New observational constraints for atmospheric hydroxyl on global and hemispheric scales, Science, 288, 500–503, 2000. 8033

ACPD
13, 8023–8064, 2013

Montzka, S., Krol, M., Dlugokencky, E., Hall, B., Jöckel, P., and Lelieveld, J.: Small interannual variability of global atmospheric hydroxyl, Science, 331, 67–69, 2011. 8033

Olivier, J. and Berdowski, J.: Global emission sources and sinks, in: The Climate System, edited by: Berdowski, J., Guicherit, R., and, Heij, B. J., 33–78, A.A. Balkema Publishers/Swets and Zeitlinger Publishers, Lisse, the Netherlands, ISBN 90 5809 255 0, 2001. 8031, 8055

Parker, R., Boesch, H., Cogan, A., Fraser, A., Feng, L., Palmer, P., Messerschmidt, J., Deutscher, N., Griffith, D., Notholt, J., Wennberg, P. O., and Wunch, D.: Methane observations from the Greenhouse gases observing SATellite: comparison to ground-based TCCON data and model calculations, Geophys. Res. Lett., 38, L15807, doi:10.1029/2011GL047871, 2011. 8034

Patra, P. K., Houweling, S., Krol, M., Bousquet, P., Belikov, D., Bergmann, D., Bian, H., Cameron-Smith, P., Chipperfield, M. P., Corbin, K., Fortems-Cheiney, A., Fraser, A., Gloor, E., Hess, P., Ito, A., Kawa, S. R., Law, R. M., Loh, Z., Maksyutov, S., Meng, L., Palmer, P. I., Prinn, R. G., Rigby, M., Saito, R., and Wilson, C.: TransCom model simulations of CH_4 and related species: linking transport, surface flux and chemical loss with CH_4 variability in the troposphere and lower stratosphere, Atmos. Chem. Phys., 11, 12813–12837, doi:10.5194/acp-11-12813-2011, 2011. 8048

Pison, I., Bousquet, P., Chevallier, F., Szopa, S., and Hauglustaine, D.: Multi-species inversion of CH_4, CO and H_2 emissions from surface measurements, Atmos. Chem. Phys., 9, 5281–5297, doi:10.5194/acp-9-5281-2009, 2009. 8031, 8032

Prinn, R., Huang, J., Weiss, R., Cunnold, D., Fraser, P., Simmonds, P., McCulloch, A., Harth, C., Reimann, S., Salameh, P., O'Doherty, S., Wang, R. H. J., Porter, L. W., Miller, B. R., and Krummel, P. B.: Evidence for variability of atmospheric hydroxyl radicals over the past quarter century, Geophys. Res. Lett, 32, L07809, doi:10.1029/2004GL022228, 2005. 8033

Ridgwell, A., Marshall, S., and Gregson, K.: Consumption of atmospheric methane by soils: a process-based model, Global Biogeochem. Cy., 13, 59–70, 1999. 8031, 8055

Rigby, M., Prinn, R., Fraser, P., Simmonds, P., Langenfelds, R., Huang, J., Cunnold, D., Steele, L., Krummel, P., Weiss, R., O'Doherty, S., Salameh, P. K., Wang, H. J., Harth, C. M., Mühle, J., and Porter, L. W.: Renewed growth of atmospheric methane, Geophys. Res. Lett., 35, L22805, doi:10.1029/2008GL036037, 2008. 8026

Sanderson, M.: Biomass of termites and their emissions of methane and carbon dioxide: a global database, Global Biogeochem. Cy., 10, 543–557, 1996. 8031, 8055

ACPD
13, 8023–8064, 2013

Spahni, R., Wania, R., Neef, L., van Weele, M., Pison, I., Bousquet, P., Frankenberg, C., Foster, P. N., Joos, F., Prentice, I. C., and van Velthoven, P.: Constraining global methane emissions and uptake by ecosystems, Biogeosciences, 8, 1643–1665, doi:10.5194/bg-8-1643-2011, 2011. 8034

van der Werf, G. R., Randerson, J. T., Giglio, L., Collatz, G. J., Mu, M., Kasibhatla, P. S., Morton, D. C., DeFries, R. S., Jin, Y., and van Leeuwen, T. T.: Global fire emissions and the contribution of deforestation, savanna, forest, agricultural, and peat fires (1997–2009), Atmos. Chem. Phys., 10, 11707–11735, doi:10.5194/acp-10-11707-2010, 2010. 8031, 8055

ACPD
13, 8023–8064, 2013

Table 1. Global annual prior methane emissions used in all the inversions.

Emissions	Tg yr^{-1}	Source
Anthropogenic emissions	364	EDGAR v4.2 Olivier and Berdowski (2001)
Biomass burning	14	GFED v3 van der Werf et al. (2010)
Termites	20	Sanderson (1996)
Ocean	17	Lambert and Schmidt (1993)
Wetlands	177	Kaplan (2002)
Soil	−38	Ridgwell et al. (1999)
Total	554	

ACPD
13, 8023–8064, 2013

Table 2. Global emissions, chemical losses, growth rates of methane and mean-bias to surface measurements. XX_{α}^{γ} where XX is a two letter code specific to each observing system (SC for SCIAMACHY, TA for TANSO-FTS, IA for IASI and SU for surface sites); α and γ are the multiplicative factors associated with the covariance matrices **B** (see Sect. 3.1) and **R** (see Sect. 3.3).

Name	Emissions $Tg\,yr^{-1}$	Loss $Tg\,yr^{-1}$	Growth Rate $Tg\,yr^{-1}$	Mean-Bias ppb
PRIOR	554	535	19	
SU_1^1	535	518	17	
$SU_1^{0.6}$	538	519	19	
SC_1^1	578	527	51	27.0
$SC_1^1C_{AF}$	603	542	61	4.7
$SC_{0.175}^{0.6}$	615	552	63	37.5
TA_1^1	576	537	39	4.6
$TA_1^1C_{AF}$	570	534	36	1.2
$TA_{0.125}^{0.6}$	568	535	33	0.5
$TA_{0.075}^{0.6}$	564	546	18	4.6
IA_1^1	531	529	2	15.1
$IA_1^{0.6}$	516	519	–3	16.3
$IA_{0.33}^{0.6}$	524	524	0	7.8

ACPD
13, 8023–8064, 2013

Table 3. Ratios (no unit) of the observation ($ratio_o$), prior ($ratio_b$), full (ratio) and analysis ($ratio_a$) variances inferred from the diagnostics. These quantities are respectively defined as the ratios between prescribed (var_o, var_b, $var = \sqrt{var_o^2 + var_b^2}$ and var_a) and associated diagnosed ($diag_o$, $diag_b$, diag and $diag_a$) error variances and represent the goodness of the error statistics in the inversion system. Good statistical consistency is obtained when the ratios are close to 1.

Name	$ratio_o$	$ratio_b$	$ratio_a$	ratio
SU_1^1	0.92	2.02	0.88	1.92
$SU_1^{0.6}$	0.74	1	0.89	0.95
SC_1^1	4.62	0.99	0.66	4.21
$SC_1^{0.6}$	4.53	0.63	1.07	4.17
$SC_{0.2}^{0.6}$	1.08	0.64		1.02
TA_1^1	9.23	0.72	0.71	4.88
$TA_1^{0.6}$	8.9	0.49	1.07	4.86
$TA_{0.125}^{0.6}$	1.35	0.48	1.11	0.82
$TA_{0.075}^{0.6}$	1.21	0.85		1.05
IA_1^1	4.07	2.33	2.47	3.4
$IA_1^{0.6}$	4.01	0.69	0.28	2.85
$IA_{0.33}^{0.6}$	1.93	0.68	0.27	1.46

ACPD
13, 8023–8064, 2013

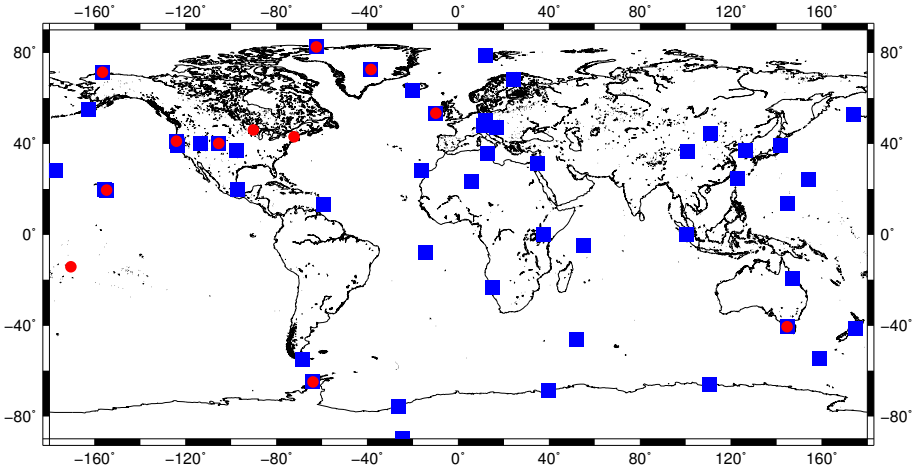

Fig. 1. Surface sites from the NOAA, ENEA, CSIRO, JMA and NIWA networks used in this study with red circles for surface sites observing MCF dry air mole fractions and blue squares for surface sites observing CH_4 dry air mole fractions.

ACPD
13, 8023–8064, 2013

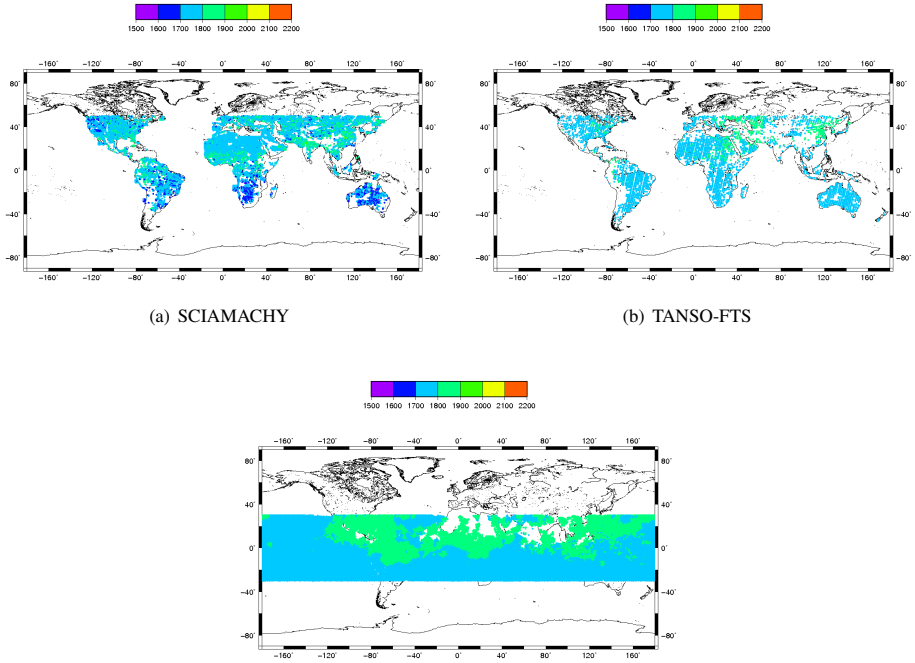

(a) SCIAMACHY (b) TANSO-FTS

(c) IASI

Fig. 2. Satellite observations (ppb) selected for the inversions for July 2010.

ACPD
13, 8023–8064, 2013

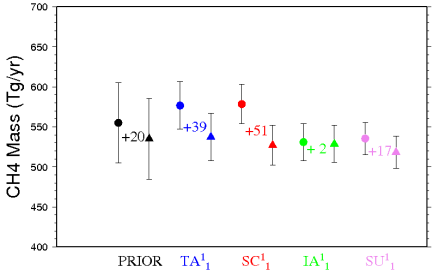

(a) Global emissions (circles) and losses (triangles) for initial configurations TA_1^1 (blue), SC_1^1 (red), IA_1^1 (green) and SU_1^1 (violet). Numbers describe the global growth rates inferred by the inversions. Error bars represent the posterior uncertainties estimated with the Monte-Carlo study (see Section 2.1)

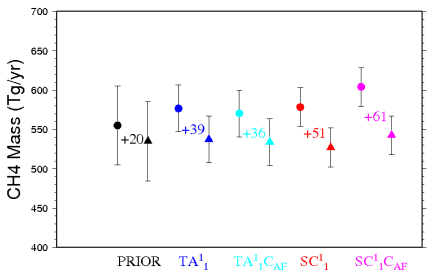

(b) Global emissions (circles) and losses (triangles) for configurations TA_1^1 (dark blue), SC_1^1 (red) and bias-corrected configurations $TA_1^1C_{AF}$ (light blue) and $SC_1^1C_{AF}$ (magenta) with numbers for global growth rates and error bars for posterior uncertainties

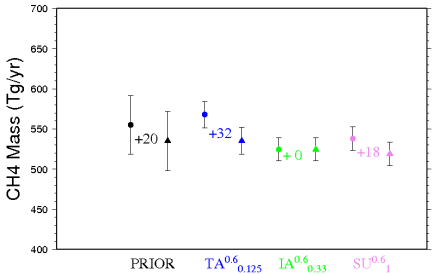

(c) Global emissions (circles) and losses (triangles) for the best configurations of the study $TA^{0.6}_{0.125}$ (blue), $IA^{0.6}_{0.33}$ (green), $SU_1^{0.6}$ (violet) with numbers for global growth rates and error bars for posterior uncertainties

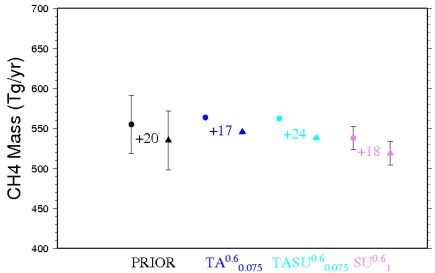

(d) Global emissions (circles and losses (triangles for configurations $TA^{0.6}_{0.075}$ (blue), $SU_1^{0.6}$ (violet) and a combination of TANSO-FTS and surface sites over 50° from the Equator $TASU^{0.6}_{0.075}$ (light blue) with numbers for global growth rates and error bars for posterior uncertainties

Fig. 3. Global methane emissions, chemical losses and growth rates inferred by the inversions.

ACPD
13, 8023–8064, 2013

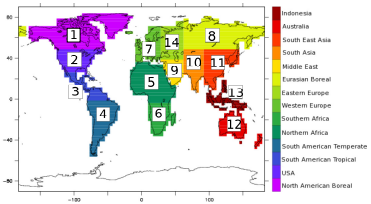

(a) Sub-continental regions inspired from Gurney et al. (2002)

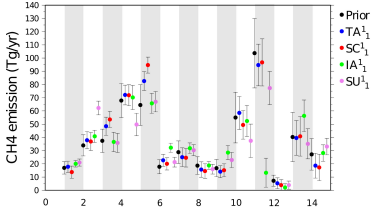

(b) Regional methane emissions for initial configurations TA^1_1 (blue), SC^1_1 (red), IA^1_1 (green) and SU^1_1 (violet). Error bars represent the posterior uncertainties estimated with the Monte-Carlo study (see Section 2.1)

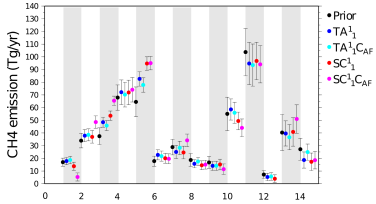

(c) Regional methane emissions for configurations TA^1_1 (dark blue), SC^1_1 (red) and bias-corrected configurations $TA^1_1C_{AF}$ (light blue) and $SC^1_1C_{AF}$ (magenta) with error bars for posterior uncertainties

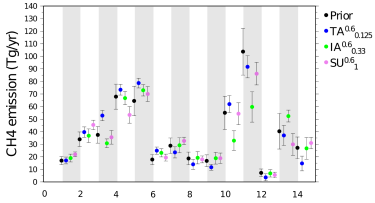

(d) Regional methane emissions for the best configurations of the study $TA^{0.6}_{0.125}$ (blue), $IA^{0.6}_{0.33}$ (green), $SU^{0.6}_1$ (violet) with error bars for posterior uncertainties

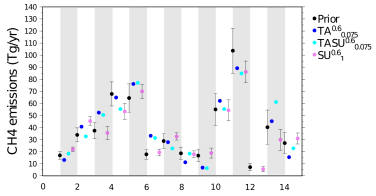

(e) Regional methane emissions for configurations $TA^{0.6}_{0.075}$ (blue), $SU^{0.6}_1$ (violet) and a combination of TANSO-FTS and surface sites over 50° from the Equator $TASU^{0.6}_{0.075}$ (light blue) with error bars for posterior uncertainties

Fig. 4. Regional methane emissions inferred by the inversions.

ACPD
13, 8023–8064, 2013

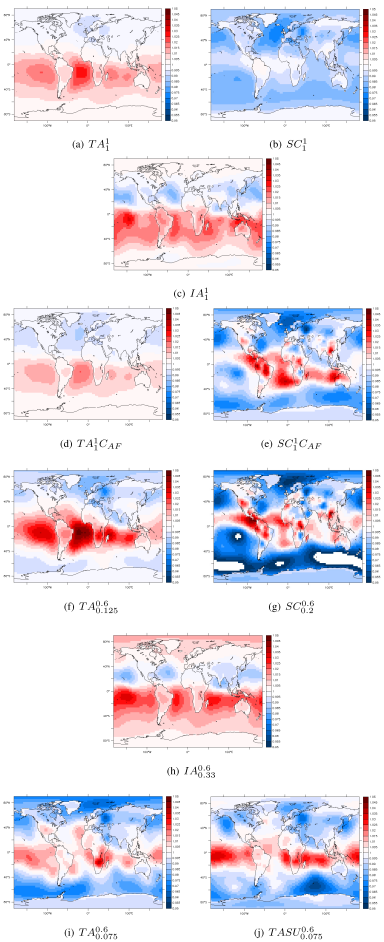

Fig. 5. Variations of the initial conditions of methane during the inversions.

ACPD
13, 8023–8064, 2013

On the consistency between global and regional methane emissions

C. Cressot et al.

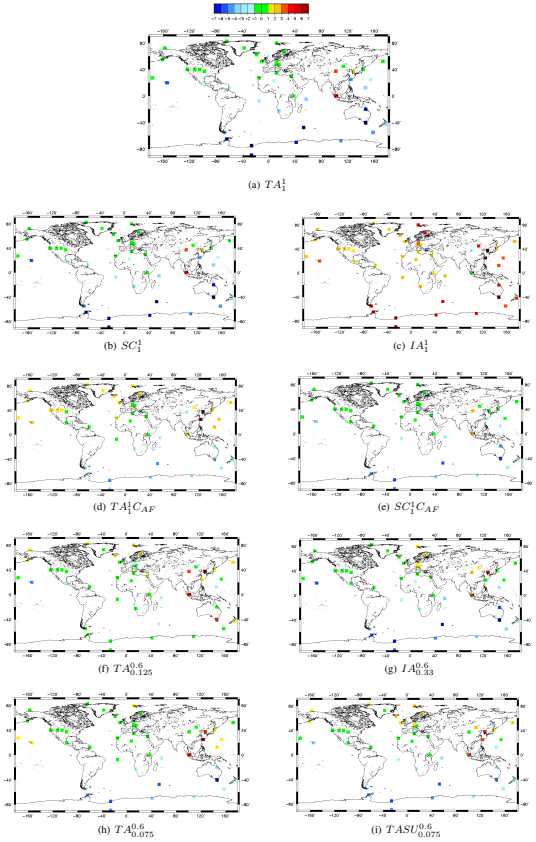

Fig. 6. Fit at surface sites represented as the ratio between posterior and prior biases to surface measurements. In green when the inversion has improved the fit to surface sites, in red when biases are too large and in blue when biases are too large (with negative values).

ACPD
13, 8023–8064, 2013

On the consistency between global and regional methane emissions

C. Cressot et al.

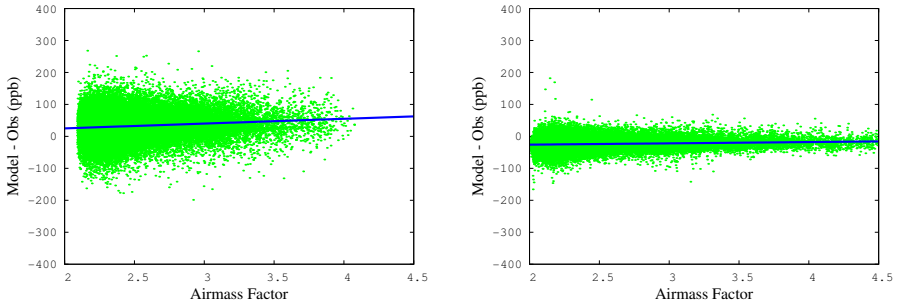

(a) Linear regression for SU_1^1 posterior state minus SCIAMACHY observations as a function of the Airmass Factor (A_F)

(b) Linear regression for $SU_1 1$ posterior state minus TANSO-FTS observations as a function of the Airmass Factor (A_F)

Fig. 7. Airmass-factor-dependent bias correction of the SCIAMACHY and TANSO-FTS observations.

ACPD
13, 8023–8064, 2013